Key Points:
- The whistler wave dispersion relation is measured for the first time by using correlation between multiple spacecraft
- The whistler wave propagating toward the X line is generated by temperature anisotropy in the electron tail
- Positive correlations between LHDI and whistler activities suggest that the anisotropy is generated by transport due to LHDI

Correspondence to:
J. Yoo,
jyoo@pppl.gov

Whistler Wave Generation by Anisotropic Tail Electrons During Asymmetric Magnetic Reconnection in Space and Laboratory

Jongsoo Yoo[1] [ID], **J. Jara-Almonte**[1] [ID], **Evan Yerger**[1] [ID], **Shan Wang**[2] [ID], **Tony Qian**[3] [ID], **Ari Le**[4] [ID], **Hantao Ji**[1] [ID], **Masaaki Yamada**[1] [ID], **William Fox**[1] [ID], **Eun-Hwa Kim**[1] [ID], **Li-Jen Chen**[2] [ID], and **Daniel J. Gershman**[2] [ID]

[1]Princeton Plasma Physics Laboratory, Princeton, NJ, USA, [2]NASA Goddard Space Flight Center, Greenbelt, MD, USA, [3]Department of Physics, Columbia University, New York, NY, USA, [4]Los Alamos National Laboratory, Los Alamos, NM, USA

Abstract Whistler wave generation near the magnetospheric separatrix during reconnection at the dayside magnetopause is studied with data from the Magnetospheric Multiscale mission. The dispersion relation of the whistler mode is measured for the first time near the reconnection region in space, which shows that whistler waves propagate nearly parallel to the magnetic field line. A linear analysis indicates that the whistler waves are generated by temperature anisotropy in the electron tail population. This is caused by loss of electrons with a high velocity parallel to the magnetic field to the exhaust region. There is a positive correlation between activities of whistler waves and the lower hybrid drift instability both in laboratory and space, indicating the enhanced transport by lower hybrid drift instability may be responsible for the loss of electrons with a high parallel velocity.

Plain Language Summary Magnetic reconnection is a fundamental process in magnetized plasma, during which magnetic energy is converted to particle energy. Due to this nature of magnetic reconnection, there are many free energy sources that can excite plasma waves such as lower hybrid and whistler waves. Whistler waves near the boundary between the magnetosphere and the exhaust region of magnetic reconnection have been observed over many decades. However, the propagation characteristic and the exact excitation mechanism associated with magnetic reconnection have not been well understood. Here the dispersion relation of the whistler wave is clearly measured for the first time by using correlations between four satellites of the Magnetospheric Multiscale mission. The measured dispersion shows that the whistler wave propagates mostly parallel to the background magnetic field toward the central reconnection region, which agrees well with a linear theory. A linear calculation with the measured electron distribution function verifies that the whistler wave is excited by temperature anisotropy in energetic electrons whose energy is much larger than that of bulk electrons. Observations both in space and laboratory suggest that lower hybrid drift instabilities may cause the anisotropy in energetic electrons, which is an interesting wave-wave-particle phenomenon.

1. Introduction

Magnetic reconnection facilitates rapid release of magnetic energy through topological rearrangement of magnetic field lines. Magnetic reconnection also mediates mixing of two different magnetized plasmas. When the two plasmas have vastly different plasma parameters, the asymmetry across the current sheet significantly affects the reconnection dynamics (Mozer & Pritchett, 2011). A classic example of asymmetric reconnection is reconnection at the dayside magnetopause, where the high-density, low-temperature solar wind plasma interacts with the low-density, high-temperature magnetospheric plasma.

Various waves have been observed during asymmetric reconnection in both the laboratory and space. In particular, fluctuations driven by lower hybrid drift instability (LHDI; Krall & Liewer, 1971) have been widely studied (Carter et al., 2001; Graham et al., 2014, 2017; Ji et al., 2004; Le et al., 2017; Mozer et al., 2011; Pritchett et al., 2012; Roytershteyn et al., 2012; Vaivads et al., 2004; Yoo et al., 2017, 2014). LHDI-driven fluctuations exist near the separatrices on the magnetospheric side (Graham et al., 2014, 2017; Le et al., 2017; Mozer et al., 2011; Price et al., 2016; Pritchett et al., 2012; Roytershteyn et al., 2012; Yoo et al., 2014, 2017), where large density gradients serve as a free energy source for LHDI. Recently, it has been concluded that LHDI-driven fluctuations enhance the electron transport and heating near the separatrix region (Le et al., 2017).
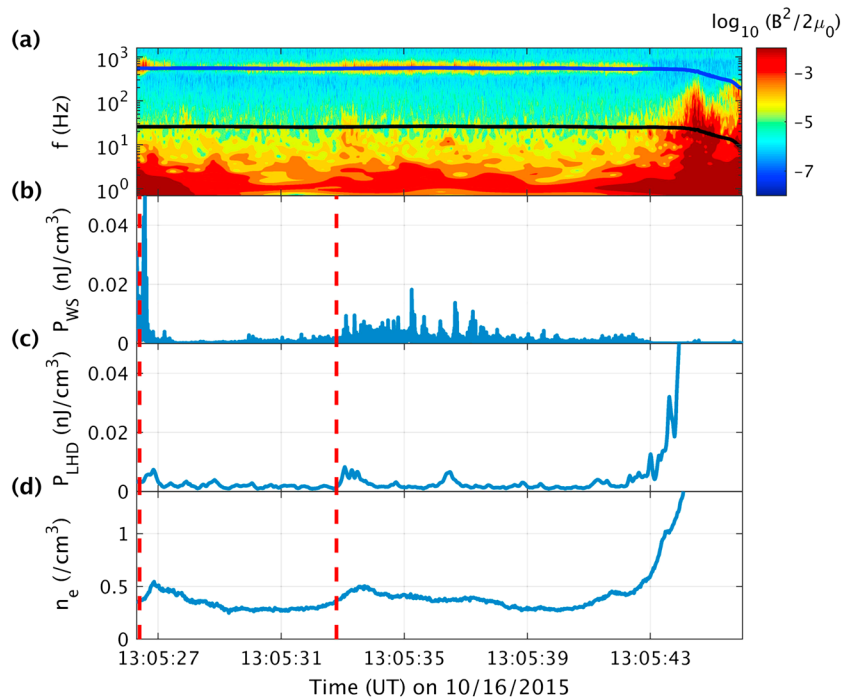
Figure 1. Whistler wave activity during asymmetric reconnection observed by MMS3. (a) Magnetic field spectrogram. The blue line indicates $0.5f_{ce}$, while the black line denotes f_{LH}. Clear whistler activity near $0.5f_{ce}$ is shown before the spacecraft crosses the separatrix around 13:05:43. Time evolution of (b) power in the whistler mode (P_{WS}), (c) power in LHDI (P_{LHD}), and (d) electron density (n_e). Red dashed lines in (b)–(d) indicate the time where P_{WS}, P_{LHD}, and n_e start to increase. LHDI = lower hybrid drift instability.

Whistler waves have been frequently observed during asymmetric reconnection in space (Cao et al., 2017; Graham et al., 2016; Le Contel, Retinó, et al., 2016; Tang et al., 2013; Wilder et al., 2016, 2017) and in laboratory (Fox et al., 2010; Jara-Almonte, 2016). Graham et al. (2016) presented that whistler waves near the magnetospheric separatrix were generated by a loss cone electron distribution. Le Contel, Retinó, et al. (2016) suggested that the perpendicular temperature anisotropy ($T_\perp > T_\parallel$) of magnetospheric energetic electrons was the free energy source of the whistler mode. Wilder et al. (2017) also suggested that whistler waves in the magnetosphere were driven by electron anisotropy. Despite these observations, the dispersion relation of the whistler wave, which is the key to understand its propagation, has never been measured. Moreover, the generation of electron temperature anisotropy during reconnection still remains as an open question.

We present the first direct measurement of the dispersion relation of the whistler mode with Magnetospheric Multiscale (MMS) data from an encounter reported by Burch et al. (2016). Moreover, the measured electron distribution function is modeled to solve the local dispersion relation and the growth rate, which confirms that the perpendicular temperature anisotropy of tail electrons generates the whistler wave. Here tail electrons are electrons with a speed much higher than the electron thermal velocity. Finally, we show that the temperature anisotropy is caused by the loss of high parallel velocity electrons to the exhaust region, which is likely due to enhanced transport of these electrons by LHDI.

2. Observation and Dispersion Relation of the Wave Activity

High-resolution burst mode data from MMS are used to study whistler wave activity during a well-known event on 16 October 2015 (Burch et al., 2016). Figure 1a shows a power spectrogram of the magnetic field measured by the Search-Coil Magnetometer (SCM) (Le Contel, Leroy, et al., 2016). The blue line indicates half of the local electron cyclotron frequency ($0.5f_{ce}$), while the black line denotes the lower hybrid frequency (f_{LH}). Clear wave activity near $0.5f_{ce}$ exists before MMS3 crosses the magnetospheric separatrix around 13:05:43. The crossing time of the separatrix can be inferred from decrease of the local electron cyclotron frequency and sharp increase of the electron density (n_e), as shown in Figure 1d. It is worth noting that the power in LHDI-driven fluctuations ($f \lesssim f_{LH}$) increases significantly at the separatrix, which is consistent

with previous studies (Graham et al., 2014, 2017; Le et al., 2017; Mozer et al., 2011; Price et al., 2016; Pritchett et al., 2012; Roytershteyn et al., 2012; Yoo et al., 2014, 2017).

Figures 1b–1d show a time evolution of the power in the wave mode, P_{WS} ($0.25f_{ce} < f < 0.75f_{ce}$), the power in LHD, P_{LHD} ($0.3f_{LH} < f < 1.4f_{LH}$), and electron density, n_e, respectively. As shown in Figure 1d, the local electron density starts to increase around 13:05:26.5 and 13:05:33, which is indicated by red dashed lines. These density increases are caused by the transport of magnetosheath electrons from the exhaust region by LHDI (Le et al., 2017). This observation is supported by simultaneous increase of low-energy electron phase space density (Figure 3c). Furthermore, the correlation between P_{LHD} and n_e also supports the transport of magnetosheath electrons by LHDI; as shown in Figures 1c and 1d, the local density increase follows peaks in P_{LHD}. For reference, the unperturbed density of the magnetosphere for this event is 0.3 cm^{-3}. The wave mode activity also correlates with both P_{LHD} and n_e. As shown in Figure 1b, P_{WS} significantly increases just after P_{LHD} and n_e start to increase.

To confirm the observed wave mode, we analyze SCM data from 13:05:26.5 to 13:05:27, using Capon's maximum-likelihood method (Capon, 1969). It employs statistics from multiple spatial measurements to estimate the underlying signal (Capon, 1983). The basic assumption is that each wave mode propagates across all measurement points as a simple plane wave, while each measurement point is subject to Gaussian noise independently.

We consider magnetic field data $B_{qj}(t)$, representing the qth component of the magnetic field according to the jth MMS. For ensemble averaging, B_{qj} is partitioned into multiple segments. Then, the Fourier transform of the nth segment is expressed as

$$b_{qjn}(\omega) = \sum_{m=1}^{N_p} B_{qj}(t_{nm}) \exp[i(m-1)\omega/2\pi f_s],$$ (1)

where $N_p = 512$ is the number of data points and $f_s = 8192$ Hz is the SCM sampling frequency.

With b_{qjn}, a 4 × 4 matrix of cross-power spectral densities can be defined:

$$S_{qjl}(\omega) = \frac{1}{N_s} \sum_{n=1}^{N_s} b_{qjn}(\omega) b_{qln}^*(\omega),$$ (2)

where $N_s = 64$ is the number of segments and b_{qln}^* is the complex conjugate of b_{qln}. Here the conventional power spectrum $P(\omega, k_p)$ is

$$P(\omega, \mathbf{k}) = \frac{1}{N_m^2} \sum_{q=1}^{3} \sum_{j,l=1}^{N_m} S_{qjl}(\omega) \exp[-i\mathbf{k} \cdot (\mathbf{x}_j - \mathbf{x}_l)],$$ (3)

where $N_m = 4$ is the number of measurement points, $\mathbf{k}$ is the wave number vector, and $\mathbf{x}_j$ is the location of the jth MMS. This power spectrum examines the phase difference of the signal between two measurement points (Beall et al., 1982). If there is a coherent wave mode across measurement points, $P(\omega, \mathbf{k})$ will reveal the frequency and wave vector of the mode.

Although this spectral density can be used to identify the wave vector, we use the maximum likelihood spectral power spectra, $P'(\omega, k_p)$ that is defined

$$P'(\omega, \mathbf{k}) = \sum_{q=1}^{3} \left[\sum_{j,l=1}^{N_M} Q_{qjl}(\omega) \exp[-i\mathbf{k} \cdot (\mathbf{x}_j - \mathbf{x}_l)] \right]^{-1},$$ (4)

where Q_{qjl} is the inverse matrix of S_{qjl}. The advantage of $P'(\omega, \mathbf{k})$ is that its variance is significantly lower than that of $P(\omega, \mathbf{k})$ (Capon, 1983; Narita et al., 2017). Using P' instead of P gives us a large advantage to clearly demonstrate the dispersion relation, since there are only four measurement points.

Figure 2a shows $P'(\omega, k_L)$ with $k_M = k_N = 0$, demonstrating a clear dispersion relation of the whistler mode. Here k_L represents $k_\parallel$, the wave number along the magnetic field direction, since in the LMN coordinate system the average magnetic field during the measurement time is $\mathbf{B}_0 = (39.0, -3.0, 3.3)$ nT. The magenta dashed line indicates the cold plasma dispersion relation with $n_e = 0.52$cm^{-3}. The red line is the dispersion relation from a dispersion solver, WHAMP (waves in homogeneous, anisotropic, multicomponent plasmas; Rönnmark, 1982),
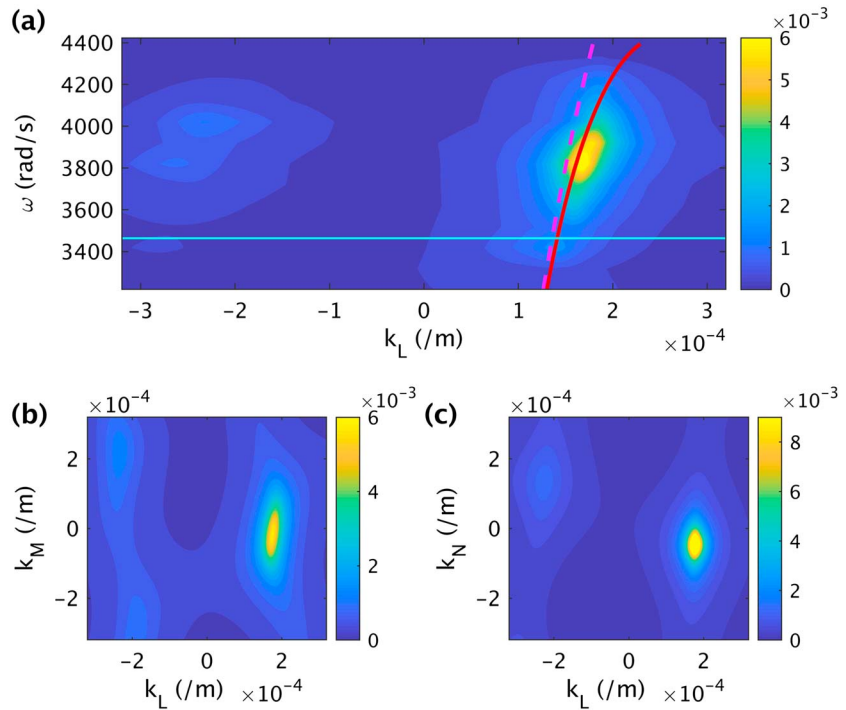
Figure 2. Maximum likelihood power spectrum for Magnetospheric Multiscale data. (a) $P'(\omega, k_L)$ with $k_M = k_N = 0$. Here k_L represents $k_\parallel$. The horizontal cyan line indicates $0.5\omega_{ce}$ with $\omega_{ce} = 2\pi f_{ce}$. The magenta dashed line is the cold plasma dispersion relation of whistler waves with $\theta = 0$. The measured dispersion agrees with the red line, which is the dispersion relation calculated by waves in homogeneous, anisotropic, multicomponent plasmas. (b) $P'(k_L, k_M)$ with $\omega = 3,921$ rad/s and $k_N = 0$. It peaks at $(k_L, k_M) = (1.75, -0.16) \times 10^{-4}$ m^{-1}. (c) $P'(k_L, k_N)$ with $\omega = 3,921$ rad/s and $k_M = 0$. It peaks at $(k_L, k_N) = (1.76, -0.45) \times 10^{-4}$ m^{-1}.

which agrees with the measured dispersion. The difference between the cold plasma dispersion and that from the WHAMP analysis means that effects from the electron temperature and flow velocity are important.

Figures 2c and 2d show $P'(k_L, k_M)$ with $k_N = 0$ and $P'(k_L, k_N)$ with $k_M = 0$ for $\omega = 3,921$ rad/s, respectively. The wave vector with the highest power at $\omega = 3,921$ rad/s is $\mathbf{k} = (1.76, -0.16, -0.45) \times 10^{-4}$ m^{-1}. In this case, θ (the angle between $\mathbf{k}$ and $\mathbf{B}_0$) is about 19°. Since MMS passed through the southern part of the X line structure (Burch et al., 2016), the relatively small θ and positive k_L mean that whistler waves propagate toward the X line almost parallel to the magnetic field, which agrees with the previous research (Le Contel, Retinó, et al., 2016). The phase velocity of the whistler mode is estimated to be about 2×10^7 m/s. The polarization of the wave from the singular value decomposition analysis (Santolík et al., 2003) is right handed.

The observed characteristics of whistler waves such as the dominant $k_\parallel$ are consistent with anisotropy-driven whistlers (Kennel & Petschek, 1966; Le Contel, Retinó, et al., 2016; Wilder et al., 2017). In this case, the whistler wave is generated by electrons with $T_\perp > T_\parallel$ at a parallel resonant velocity, V_{res}. The cyclotron resonance occurs when the Doppler-shifted frequency of the wave is ω_{ce} (Kennel & Petschek, 1966), which is

$$\omega - V_{res} k_\parallel = \omega_{ce}. \tag{5}$$

With $\theta = 0$ and $k_\parallel > 0$, the cold plasma dispersion relation ($kd_e = \sqrt{\omega/(\omega_{ce} \cos \theta - \omega)}$; $d_e = c/\omega_{pe}$ is the electron skin depth; ω_{pe} is the electron plasma frequency) gives us

$$V_{res} = -V_{Ae}(1 - \omega/\omega_{ce})^{1.5}(\omega/\omega_{ce})^{-0.5}, \tag{6}$$

where $V_{Ae} = c(\omega_{ce}/\omega_{pe})$ is the electron Alfvén velocity. The magnitude of V_{res} monotonically decreases as ω increases. Note that the sign of V_{res} is the opposite to the parallel phase velocity ($V_{ph\parallel} \equiv \omega/k_\parallel$). This means that we need to look at electron populations with a negative parallel velocity to understand the generation of whistlers with $V_{ph} > 0$. Equation (6) also implies that tail electrons are responsible for the whistler wave generation because $V_{Ae} \approx 14 v_{the}$ in this region, where $v_{the} \equiv \sqrt{kT_e/m_e}$ is the electron thermal velocity. For $0.5\omega_{ce} < \omega < 0.6\omega_{ce}$, $|V_{res}|$ ranges from $4 v_{the}$ to $7 v_{the}$.
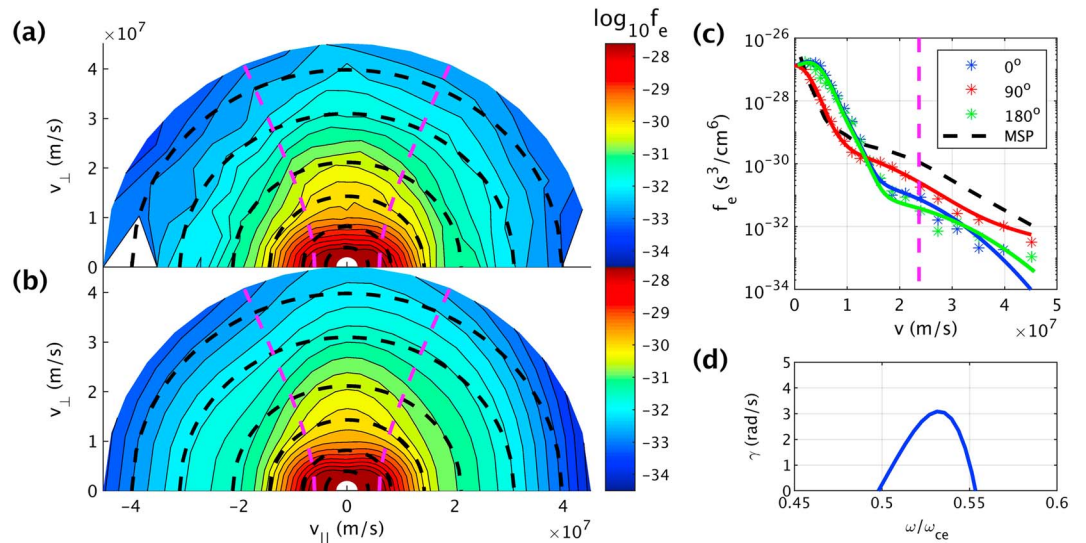
Figure 3. (a) Two-dimensional electron distribution function ($f_e(v_{\parallel}, v_{\perp})$) measured by MMS3 from 13:05:26.5 to 13:05:27. Black dashed semicircles represent sample contours of an isotropic f_e. Magenta dashed lines indicate boundaries between trapped and passing electrons. (b) Modeled 2-D electron distribution function for the waves in homogeneous, anisotropic, multicomponent plasmas analysis. (c) One-dimensional distribution functions for $\phi = 0°$ (blue), 90° (red), and 180° (green), where ϕ is the pitch angle. Solid lines are results from the modeling. The black dashed line is a reference distribution function averaged over the pitch angle. This reference distribution function is obtained in the magnetoshpere (MSH) further away from the separatrix region. The magenta dashed line denotes the resonance velocity for $\omega \sim 0.55\omega_{ce}$. (d) Growth rate calculated by waves in homogeneous, anisotropic, multicomponent plasmas.

3. Distribution Function and Linear Analysis

Figure 3a shows the 2-D electron distribution function measured by the Fast Plasma Investigation (FPI) (Pollock et al., 2016). For electrons with a low speed ($v_e < 3v_{the}$; v_e is the electron speed; $v_{the} \sim 4 \times 10^6$ m/s), contours of the phase space density (f_e) are elongated along the parallel direction, indicating $T_{\parallel} > T_{\perp}$ for these electrons. This anisotropy is consistent with trapped particle dynamics under an acceleration potential (Egedal et al., 2008). The magenta dashed lines denote the boundaries between trapped and passing electrons, based on the anticipated acceleration potential and magnitude of the magnetic field far from the reconnection region; electrons between the lines are trapped due to the parallel electric field and magnetic mirror force. For tail electrons ($v_e > 3v_{the}$), however, the trend is reversed; contours are elongated along the perpendicular direction. These tail electrons with $T_{\perp} > T_{\parallel}$ excite the whistler mode (Gary & Wang, 1996; Kennel & Petschek, 1966).

To confirm this argument, WHAMP has been employed to obtain the dispersion relation and growth rate. Due to constraint in the solver, the local 2-D electron distribution function must be modeled as a sum of bi-Maxwellian distribution functions. Figure 3b shows the modeled electron distribution function, which has the same key features as the measured distribution function. The combined electron density and parallel flow velocity (~270 km/s) also match to measured values.

Figure 3d shows the growth rate (γ) for $\theta = 0$ computed by WHAMP. WHAMP expects a positive growth rate for $0.5\omega_{ce} \lesssim \omega \lesssim 0.6\omega_{ce}$, which agrees with measurements. The whistler mode with negative $k_{\parallel}$, on the other hand, is marginally stable ($\gamma \sim 0$, not shown) due to resonant electrons with $|v_{\parallel}| \gg v_{\perp}$. Figure 3c clearly shows that the phase space density of electrons with resonant velocity ($|V_{res}| \approx 2$ to 3×10^7 m/s) with $\phi = 0$ (blue asterisks, resonant with whistlers with $k_{\parallel} < 0$) is higher than that with $\phi = 180°$ (green asterisks, resonant with whistlers with $k_{\parallel} > 0$). Resonant electrons with a dominant parallel velocity damp whistler waves.

There is a shoulder near the phase velocity of whistlers ($\sim 2 \times 10^7$ m/s) in $f_e(\theta = 0°$, which has been observed together with whistler waves (Wilder et al., 2016, 2017). It should be mentioned that this shoulder structure is not an electron beam exciting the whistler mode. Instead, it results from damping of waves: WHAMP calculations without the shoulder structure show that the growth rate of the whistler waves with $k_{\parallel} < 0$ becomes positive. The shoulder structure indicates that the distribution is marginally stable to the whistler mode; it also
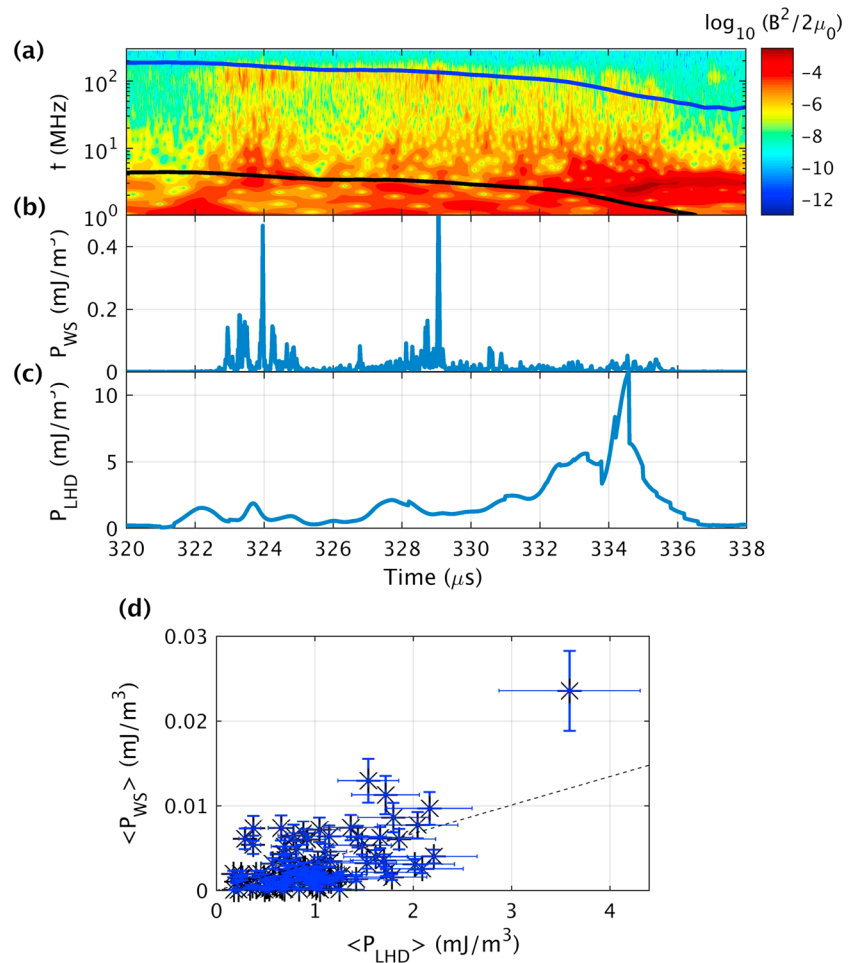
Figure 4. Magnetic Reconnection Experiment observation of whistler waves near the separatrix on the low-density side. (a) Magnetic field spectrogram by wavelet analysis. The blue and black lines indicate $0.5f_{ce}$ and f_{LH}, respectively. Time evolution of (b) power in the whistler mode and (c) power in the LHDI. (d) Statistical analysis between the power in LHDI-driven fluctuations P_{LHD} and whistlers P_{WS}. There is a positive correlation between two values with strong statistical significance. The correlation coefficient is 0.63. LHDI = lower hybrid drift instability.

exists in the electron distribution function further away from the separatrix region, where the whistler mode is marginally stable.

The electron distribution functions in Figures 3a and 3c suggest that the loss of high parallel velocity electrons to the exhaust region is the fundamental reason for the perpendicular anisotropy ($T_\perp > T_\parallel$) in the tail population. Compared to the black dashed line, which denotes a reference magnetosphere distribution function obtained further away from the separatrix region, $f_e(\theta = 90°$; red asterisks) shows decrease of the phase space density for electrons with $v_e > 2v_{th}$. The decrease of the phase space density of these trapped electrons is expected from the trapped particle dynamics (Egedal et al., 2008). The comparable phase space density for electrons with $v_e < 2v_{th}$ is caused by electrons originating in the magnetosheath. On the other hand, the phase space of high parallel velocity electrons (represented by $f_e(\theta = 0, 180°$), blue and green asterisks) with $v_e > 4v_{th}$ becomes much lower than the reference distribution. Since these electrons are not trapped, this significant loss of these electrons cannot be explained by the trapped particle dynamics. The correlative behavior between P_{WS} and P_{LHD} in Figure 1 indicates that LHDI may be responsible for the loss of electrons with a high parallel velocity.

It should be mentioned that the exact mechanism for the observed anisotropy in tail electrons requires further investigation. Besides LHDI, there is a possibility that the observed 2-D electron distribution can be explained by a model based on the double adiabatic theory (Montag et al., 2017). The measurement location is away from the X line, such that there is no significant change in the local magnetic field strength during the whistler

wave activity; the local flux tube has not been expanded. The part of the flux tube, on the other hand, may be stretched as the tube approaches the X line, resulting in the average density in the flux tube decreases. In this case, the electrons with a high parallel velocity can be dominantly cooled. However, this mechanism cannot explain the increase of the local electron density observed around UT13:05:27, which is caused by the low-energy electrons from the magnetosheath. The density increase indicates that the part of the flux tube has been already affected by the electron mixing process via LHID-driven turbulence (Le et al., 2017).

4. Laboratory Observation and Discussion

The whistler mode is also observed during asymmetric reconnection in the Magnetic Reconnection Experiment (MRX; Yamada et al., 1997). Figure 4a shows a magnetic field spectrogram from MRX data that have a remarkable similarity to that from MMS data shown in Figure 1a. It is measured by a probe that is sensitive to fluctuations in the magnetic field up to 200 MHz. The measurement location is about $1 d_i$ away from the X line along the outflow direction. Initially, it is on the low-density (magnetospheric) side and moves into the exhaust region around 336 µs, due to the natural motion of the current sheet in MRX (Yoo & Yamada, 2012).

Figures 4b and 4c demonstrate the time evolution of P_{WS} and P_{LHD}, respectively. The whistler wave activity appears after P_{LHD} increases around 322 µs. When P_{LHD} is low around 326 µs, the whistler wave activity decreases. P_{WS} becomes large again after P_{LHD} increases around 327 µs. This correlative behavior between P_{WS} and P_{LHD} supports the relation between the whistler wave and LHDI. The large P_{LHD} around $t = 334$ µs is due to the separatrix crossing.

We also perform a statistical analysis of data from 98 discharges with a large density asymmetry; the density ratio across the current sheet is about 10. Key plasma parameters on the low-density side are $n_e = 3$ to 5×10^{12} cm^{-3} and $T_e \gtrsim 7$ eV. Under these conditions, the electron mean free path (~20 cm) is comparable to the system size ($L \sim 40$ cm). As shown in Figure 4d, there is a strong correlation between $\langle P_{LHD} \rangle$ and $\langle P_{WS} \rangle$. Here $\langle P_{LHD} \rangle$ and $\langle P_{WS} \rangle$ indicate the mean value of P_{LHD} and P_{WS} during $t = 322$–332 µs, respectively. The correlation coefficient is 0.63, and the probability value for the null hypothesis is negligible ($\sim 4 \times 10^{-12}$). This positive correlation with strong statistical significance indicates that LHDI may be responsible for the whistler wave excitation.

In summary, we show that electromagnetic fluctuations ($f \sim 0.5 f_{ce}$) near the magnetospheric separatrix are whistler waves. The dispersion relation of the whistler mode is measured for the first time near the reconnection region in space and shows that it propagates toward the X line nearly parallel to the background magnetic field. WHAMP analysis verifies that the whistler waves are generated by temperature anisotropy in tail electrons. Measured electron distribution functions show that the temperature anisotropy of the tail electrons is generated by the loss of high parallel velocity electrons. The correlation between LHDI and whistler activities in both space and laboratory suggests that LHDI-driven turbulence produces enhanced transport of electrons with a high parallel velocity to the exhaust region, but the exact mechanism for the temperature anisotropy in tail electrons requires further investigation.

Whistler waves can be an important indicator of an active development of LHDI turbulence that may create anomalous resistivity in the electron diffusion region (Ji et al., 2005; Kulsrud et al., 2005; Price et al., 2016). Moreover, they can be also an indicator of the separatrix and help determine to the spacecraft location. During this research, we have also found that whistler wave activity exists near the electron diffusion region. Understanding whistler waves near the diffusion region will be the next research topic.

References

Beall, J., Kim, Y., & Powers, E. (1982). Estimation of wavenumber and frequency spectra using fixed probe pairs. *Journal of Applied Physics*, *53*(6), 933.

Burch, J. L., Torbert, R. B., Phan, T. D., Chen, L.-J., Moore, T. E., Ergun, R. E., et al. (2016). Electron-scale measurements of magnetic reconnection in space. *Science*, *352*(6290), aaf2939.

Cao, D., Fu, H. S., Cao, J. B., Wang, T. Y., Graham, D. B., Chen, Z. Z., et al. (2017). MMS observations of whistler waves in electron diffusion region. *Geophysical Research Letters*, *44*, 3954–3962. https://doi.org/10.1002/2017GL072703

Capon, J. (1969). High-resolution frequency-wavenumber spectrum analysis. *Proceedings of the IEEE*, *57*(8), 1408–1418.

Capon, J. (1983). Maximum-likelihood spectral estimation. In S. Haykin (Ed.), *Nonlinear Methods of Spectral Analysis* (pp. 155–179). New York, USA: Springer-Verlag.

Carter, T. A., Ji, H., Trintchouk, F., Yamada, M., & Kulsrud, R. M. (2001). Measurement of lower-hybrid drift turbulence in a reconnecting current sheet. *Physical Review Letters*, *88*, 015001.

Egedal, J., Fox, W., Katz, N., Porkolab, M., ØŸieroset, M., Lin, R. P., et al. (2008). Evidence and theory for trapped electrons in guide field magnetotail reconnection. *Journal of Geophysical Research*, *113*, A12207. https://doi.org/10.1029/2008JA013520

Fox, W., Porkolab, M., Egedal, J., Katz, N., & Le, A. (2010). Laboratory observations of electron energization and associated lower-hybrid and Trivelpiece-Gould wave turbulence during magnetic reconnection. *Physics of Plasmas*, *17*(7), 072303.

Gary, S. P., & Wang, J. (1996). Whistler instability: Electron anisotropy upper bound. *Journal of Geophysical Research*, *101*(A5), 10,749–10,754.

Graham, D. B., Khotyaintsev, Y. V., Norgren, C., Vaivads, A., André, M., Toledo-Redondo, S., et al. (2017). Lower hybrid waves in the ion diffusion and magnetospheric inflow regions. *Journal of Geophysical Research: Space Physics*, *122*, 517–533. https://doi.org/10.1002/2016JA023572

Graham, D. B., Khotyaintsev, Y. V., Vaivads, A., André, M., & Fazakerley, A. N. (2014). Electron dynamics in the diffusion region of an asymmetric magnetic reconnection. *Physical Review Letters*, *112*, 215004.

Graham, D. B., Vaivads, A., Khotyaintsev, Y. V., & André, M. (2016). Whistler emission in the separatrix regions of asymmetric magnetic reconnection. *Journal of Geophysical Research: Space Physics*, *121*, 1934–1954. https://doi.org/10.1002/2015JA021239

Jara-Almonte, J. (2016). Multiple-scale physics during magnetic reconnection (Ph.D. thesis), Princeton University.

Ji, H., Kulsrud, R., Fox, W., & Yamada, M. (2005). An obliquely propagating electromagnetic drift instability in the lower hybrid frequency range. *Journal of Geophysical Research*, *110*, A08212. https://doi.org/10.1029/2005JA011188

Ji, H., Terry, S., Yamada, M., Kulsrud, R., Kuritsyn, A., & Ren, Y. (2004). Electromagnetic fluctuations during fast reconnection in a laboratory plasma. *Physical Review Letters*, *92*, 115001.

Kennel, C. F., & Petschek, H. E. (1966). Limit on stably trapped particle fluxes. *Journal of Geophysical Research*, *71*(1), 1–28.

Krall, N. A., & Liewer, P. C. (1971). Low-frequency instabilities in magnetic pulses. *Physical Review A*, *4*, 2094–2103.

Kulsrud, R., Ji, H., Fox, W., & Yamada, M. (2005). An electromagnetic drift instability in the magnetic reconnection experiment and its importance for magnetic reconnection. *Physics of Plasmas*, *12*, 082301.

Le Contel, O., Leroy, P., Roux, A., Coillot, C., Alison, D., Bouabdellah, A., et al. (2016). The search-coil magnetometer for MMS. *Space Science Reviews*, *199*(1), 257–282.

Le Contel, O., Retinó, A., Breuillard, H., Mirioni, L., Robert, P., Chasapis, A., et al. (2016). Whistler mode waves and hall fields detected by MMS during a dayside magnetopause crossing. *Geophysical Research Letters*, *43*, 5943–5952. https://doi.org/10.1002/2016GL068968

Le, A., Daughton, W., Chen, L.-J., & Egedal, J. (2017). Enhanced electron mixing and heating in 3-D asymmetric reconnection at the earth's magnetopause. *Geophysical Research Letters*, *44*, 2096–2104. https://doi.org/10.1002/2017GL072522

Montag, P., Egedal, J., Lichko, E., & Wetherton, B. (2017). Impact of compressibility and a guide field on Fermi acceleration during magnetic island coalescence. *Physics of Plasmas*, *24*(6), 062906.

Mozer, F. S., & Pritchett, P. L. (2011). Electron physics of asymmetric magnetic field reconnection. *Space Science Reviews*, *158*(1), 119–143.

Mozer, F. S., Wilber, M., & Drake, J. F. (2011). Wave associated anomalous drag during magnetic field reconnection. *Physics of Plasmas*, *18*(10), 102902.

Narita, Y., Nishimura, Y., & Hada, T. (2017). Minimum variance projection for direct measurements of power-law spectra in the wavenumber domain. *Annales Geophysicae*, *35*(3), 639–644. https://doi.org/10.5194/angeo-35-639-2017

Pollock, C., Moore, T., Jacques, A., Burch, J., Gliese, U., Saito, Y., et al. (2016). Fast plasma investigation for Magnetospheric Multiscale. *Space Science Reviews*, *199*(1), 331–406.

Price, L., Swisdak, M., Drake, J. F., Cassak, P. A., Dahlin, J. T., & Ergun, R. E. (2016). The effects of turbulence on three-dimensional magnetic reconnection at the magnetopause. *Geophysical Research Letters*, *43*, 6020–6027. https://doi.org/10.1002/2016GL069578

Pritchett, P. L., Mozer, F. S., & Wilber, M. (2012). Intense perpendicular electric fields associated with three-dimensional magnetic reconnection at the subsolar magnetopause. *Journal of Geophysical Research*, *117*, A06212. https://doi.org/10.1029/2012JA017533

Rönnmark, K. (1982). Waves in homogeneous, anisotropic, multicomponent plasmas (Tech. Rep.) Kiruna, Sweden: Kiruna Geophys. Inst.

Roytershteyn, V., Daughton, W., Karimabadi, H., & Mozer, F. S. (2012). Influence of the lower-hybrid drift instability on magnetic reconnection in asymmetric configurations. *Physical Review Letters*, *108*, 185001.

Santolík, O., Parrot, M., & Lefeuvre, F. (2003). Singular value decomposition methods for wave propagation analysis. *Radio Science*, *38*(1), 1010. https://doi.org/10.1029/2000RS002523

Tang, C., Cattell, C., Dombeck, J., Dai, L., Wilson, L. B., Breneman, A., & Hupach, A. (2013). THEMIS observations of the magnetopause electron diffusion region: Large amplitude waves and heated electrons. *Geophysical Research Letters*, *40*, 2884–2890. https://doi.org/10.1002/grl.50565

Vaivads, A., Khotyaintsev, Y., André, M., Retinò, A., Buchert, S. C., Rogers, B. N., et al. (2004). Structure of the magnetic reconnection diffusion region from four-spacecraft observations. *Physical Review Letters*, *93*, 105001.

Wilder, F. D., Ergun, R. E., Goodrich, K. A., Goldman, M. V., Newman, D. L., Malaspina, D. M., et al. (2016). Observations of whistler mode waves with nonlinear parallel electric fields near the dayside magnetic reconnection separatrix by the Magnetospheric Multiscale mission. *Geophysical Research Letters*, *43*, 5909–5917. https://doi.org/10.1002/2016GL069473

Wilder, F. D., Ergun, R. E., Newman, D. L., Goodrich, K. A., Trattner, K. J., Goldman, M. V., et al. (2017). The nonlinear behavior of whistler waves at the reconnecting dayside magnetopause as observed by the Magnetospheric Multiscale mission: A case study. *Journal of Geophysical Research: Space Physics*, *122*, 5487–5501. https://doi.org/10.1002/2017JA024062

Yamada, M., Ji, H., Hsu, S., Carter, T., Kulsrud, R., Bretz, N., et al. (1997). Study of driven magnetic reconnection in a laboratory plasma. *Physics of Plasmas*, *4*(5), 1936–1944.

Yoo, J., Na, B., Jara-Almonte, J., Yamada, M., Ji, H., Roytershteyn, V., et al. (2017). Electron heating and energy inventory during asymmetric reconnection in a laboratory plasma. *Journal of Geophysical Research: Space Physics*, *122*, 9264–9281. https://doi.org/10.1002/2017JA024152

Yoo, J., & Yamada, M. (2012). Experimental evaluation of common spacecraft data analysis techniques for reconnection region analysis in a laboratory plasma. *Journal of Geophysical Research*, *117*, A12202. https://doi.org/10.1029/2012JA017742

Yoo, J., Yamada, M., Ji, H., Jara-Almonte, J., Myers, C. E., & Chen, L.-J. (2014). Laboratory study of magnetic reconnection with a density asymmetry across the current sheet. *Physical Review Letters*, *113*, 095002.